Research Square

Preprints are preliminary reports that have not undergone peer review.
They should not be considered conclusive, used to inform clinical practice,
or referenced by the media as validated information.

Ice contributed only 53% to the flood triggered by the 2026 Langtang Lirung rock-ice avalanche in Nepal

Lixin Wu

wulx66@csu.edu.cn

Central South University

Zhijun Jiao

Central South University

Suraj Gautam

Institute of Himalayan Risk Reduction, Lalitpur, Nepal

Raju Thapa

Nepal Center for Disaster Management, Kathmandu, Nepal

Zhimei Zhang

Central South University

Pengtianhao Wu

Central South University

Zichen Yue

School of Geosciences and Info-Physics, Central South University, Changsha, China

Qiqi Zhang

School of Geosciences and Info-Physics, Central South University, Changsha, China

Wenfei Mao

School of Geosciences and Info-Physics, Central South University, Changsha, China

Bishal Nath Upreti

Nepal Center for Disaster Management, Kathmandu, Nepal

Meen B. Poudyal Chhetri

Nepal Center for Disaster Management, Kathmandu, Nepal

Article

Keywords:

Posted Date: October 19th, 2026

DOI: https://doi.org/10.21203/rs.3.rs-11386405/v1

License: This work is licensed under a Creative Commons Attribution 4.0 International License.
Read Full License

Additional Declarations: There is **NO** Competing Interest.

Ice contributed only 53% to the flood triggered by the 2026 Langtang Lirung rock-ice avalanche in Nepal

Zhijun Jiao[a], Suraj Gautam[b], Raju Thapa[c], Zhimei Zhang[a], Pengtianhao Wu[a], Zichen Yue[a], Qiqi Zhang[a], Wenfei Mao[a], Bishal Nath Upreti[c], Meen B. Poudyal Chhetri[c], Lixin Wu[a*]

[a] School of Geosciences and Info-Physics, Central South University, Changsha, China

[b] Institute of Himalayan Risk Reduction, Lalitpur, Nepal

[c] Nepal Center for Disaster Management, Kathmandu, Nepal

*Corresponding author: Lixin Wu

School of Geosciences and Info-Physics, Central South University, 932 Lushan South Road, Yuelu District, Changsha, Hunan 410083, China

E-mail: wulx66@csu.edu.cn

Abstract

A high-mountain rock-ice collapse can generate cascading debris flows and floods beyond its source. Quantifying the materials released at the source and those added to the flood along the corridor is essential to understanding the cascading event and disaster risk. We reconstruct the 26 August 2026 Langtang Lirung avalanche using satellite imagery, terrain reconstruction, videos, seismic scaling and river-gauge records. A source volume of $78.37 \times 10^6 m^3$ and rock:ice volume ratio of 9:1 yield a mass of $1.98 \times 10^{11} kg$ and a predicted magnitude of 5.20, consistent with the USGS observation. Complete ice melting supplies at most $7.19 \times 10^6 m^3$, or 53% of the Devghat excess. Adding corridor-water storage gives $(14.42 \pm 0.80) \times 10^6 m^3$, 6.30% above the observed $13.57 \times 10^6 m^3$. The paired comparisons support debris-driven mobilization of pre-existing river water into a downstream surge. Hazard assessment and transboundary preparedness must incorporate corridor water and erodible deposits alongside unstable high-elevation sources.

Steep valley walls, large elevation differences and fractured bedrock allow high-mountain slope failures to release large masses into confined corridors. Glacier retreat and changes in frozen ground can alter slope support, water movement and rock strength, while geological structure determines where failure can develop[1,2]. Once released, rock and ice can entrain sediment and water, extending the affected area well beyond the initial collapse. Reconstructing these cascades therefore requires observations that connect the source, transport corridor and downstream response[3]. The 2021 Chamoli disaster demonstrated this cascading hazard: an ice-rock avalanche transformed into a mobile debris flow that severely damaged two hydropower projects and left more than 200 people dead or missing[4]. This cascading hazard is particularly relevant as glacier ice loss across High Mountain Asia continues amid ongoing climate warming[5,6,7,8], while sparse permafrost observations in the Hindu Kush Himalaya[2] limit our understanding of slope destabilization. With growing concerns over destructive

glacier-related slope failures[9] and the warming-related destabilization and adaptation limits highlighted by the 2026 Nepal cascade[10], understanding how these cascading hazard processes interact and propagate downstream is essential for explaining the disproportionate impacts of high-mountain disaster cascades.

Understanding why these cascading impacts extend far beyond the initial collapse requires examining how the moving mass interacts with materials and water along its path. Snow entrainment influenced the runout and air-blast generation at Langtang in 2015[11], while reconstructions in Tibet and Switzerland linked long runout to low effective friction and the presence of water or ice within the moving mass[12,13]. Experimental and field evidence further identifies water availability, corridor materials and topographic confinement as important controls on mobility[14]. Together, these studies suggest that the severity and extent of cascading hazards depend not only on the initial failed mass, but also on the progressive entrainment and transformation of materials during propagation.

Beyond the physical amplification of cascading hazards, the exposure of people and infrastructure along their propagation corridors can further magnify the consequences. Hydropower facilities, roads, bridges and settlements are often situated within narrow mountain valleys, placing them directly in the paths of avalanches, debris flows and floods[15]. The 2021 Chamoli disaster illustrates how a localized slope failure can cause extensive damage to downstream infrastructure and communities[4]. Studies of glacial-lake outburst floods similarly highlight the importance of water storage, hydrological connectivity and downstream exposure in determining disaster impacts[16,17,18,19]. The timing of flood release and the connectivity of downstream corridors further influence the distribution of these impacts[20,21,22,23], while assessments linking unstable slopes to avalanches entering stored water demonstrate how multiple processes can combine to threaten exposed areas[24]. Thus, the consequences of a cascading disaster depend not only on how hazards evolve and propagate, but also on what lies along their paths.

The interaction between cascading hazard processes and downstream exposure highlights the need to reconstruct how an initial slope failure develops into a far-reaching disaster. Process-chain modelling demonstrates that avalanche location and propagation corridor affect flood intensity[25], while studies of Blatten and Dharali establish the value of pre-event source observations for early warning and risk reduction[26,27]. Understanding these cascades therefore requires connecting the initial release, the entrainment and mobilization of materials and water along the transport corridor, and the resulting downstream response. An event-scale reconstruction must constrain both the released rock-ice mass and the water mobilized along its corridor using observations of the same event. A remaining observational challenge is to test both ends of the same cascade: whether a reconstructed rock-ice inventory is compatible with the seismic signal of release? Whether the water available along its path is compatible with a downstream hydrograph?

On 26 August 2026, a slope on the north-facing flank of Langtang Lirung failed and initiated a cascade through Lhende Khola, Bhote Koshi and the Trishuli valley, which USGS preliminarily recorded as a seismic event. Subsequent assessments documented debris-flow and flood impacts extending approximately 100km downstream, with severe damage to riverside buildings and roads connecting China and Nepal[28,29,30]. Nepal's flood technical report records the loss of upstream hydrological stations, including the Furke (Malekhu) station and its bridge, and continued observation of the flood farther downstream[31].

The far-reaching destruction caused by this event underscores a fundamental challenge in understanding high-mountain disaster cascades: how a localized rock-ice collapse can evolve into a destructive flood that threatens infrastructure and communities far beyond its source. Addressing this challenge requires moving beyond the characterization of individual hazards to quantitatively linking the initial failure, the transformation of moving materials and the mobilization of river water within a unified source-to-flood framework. Here, we reconstruct the 26 August 2026 Langtang Lirung cascade

by integrating source reconstruction, propagation evidence and a corridor-water budget (Fig. 1). Pre- and post-event imagery constrain the failure geometry (Fig. 2), while terrain reconstruction and UAV-derived composition estimates quantify the released rock-ice mass and assess its consistency with the USGS-recorded seismic magnitude (Fig. 3). Video observations reveal the sequence of flow transformations, and Knowledge-Driven Flood Intelligent Monitoring (KDFIM)-constrained water accounting evaluates the contribution of pre-existing river water against the observed Devghat flood hydrograph (Fig. 4). Sensitivity analysis across varying rock-to-ice ratios further examines the robustness of these constraints (Fig. 5). By jointly testing the source mass against seismic observations and the available water volume against downstream hydrological measurements, this study provides an observation-constrained assessment of how rock-ice avalanches can mobilize river water and amplify flood hazards far beyond the initial collapse. This framework advances the quantitative understanding of high-mountain disaster cascades and provides a basis for assessing cascading flood risks to downstream infrastructure and communities.

Imagery resolves the released rock-ice body

The source footprint was delineated by comparing pre- and post-event satellite imagery, as shown in Fig. 2. Sentinel-2 imagery acquired on 24 August 2026 shows the intact source rock-ice body, whereas Landsat-9 imagery from 26 August 2026 reveals the disappearance of the source rock-ice body and the newly exposed collapse scar (Fig. 2B, C). The reconstructed source boundary was further examined using a high-resolution image acquired on 10 October 2017 (Fig. 2D). This historical image reveals a distinctly fractured and weathered rock zone, with its structural boundaries closely matching the mapped failure footprint, as shown in the enlarged view (Fig. 2E). The agreement between the pre-existing fracture pattern and the post-event collapse geometry provides additional evidence for the identification of a rock-ice block. Repeated melting, refreezing and seasonal ice loss may have

contributed to progressive fracture opening and reduced slope support, consistent with mechanisms proposed for the destabilization of the Chamoli source[32].

Regional structural studies have documented tectonically deformed High Himalayan Gneiss in the Langtang Valley[33], providing geological context for the fractured rock mass observed in the historical imagery. These observations suggest that pre-existing structural weaknesses, potentially modified by freeze-thaw processes and ice loss, may have contributed to slope destabilization. The source geometry was therefore constrained primarily by the observed collapse scar and surrounding terrain, while rock-ice composition and density were considered separately to estimate the released mass.

Source reconstruction and seismic comparison

Integration of the source geometry constrained by the mapped outline and three reference surfaces gives a source volume of $78.37 \times 10^6 m^3$ (Fig. 3B). Field UAV image interpretation gives a rock:ice volume ratio of 9:1. With densities of 917kg m^{-3} for ice and 2700kg m^{-3} for rock[34], the bulk density is 2.52×10^3kg m^{-3} and the mass is 1.98×10^{11}kg. The empirical scaling of Ekström and Stark[35] yields a maximum force of 3.66×10^{11}N and a predicted magnitude of 5.20, matching the USGS-reported M5.20 landslide signal[29].

The three-dimensional terrain reconstruction reveals a steep and confined propagation corridor connecting the rock-ice source to Gyirong Port through Lhende Khola and Bhote Koshi (Fig. 3A). The corresponding longitudinal profile shows a pronounced elevation drop from approximately 5,152 m at the source to 1,823 m near Gyirong Port over a distance of about 20 km (Fig. 3C). The particularly steep upper section provided a substantial gravitational driving force for the initial descent, while the narrow valley geometry channelled the moving material towards the downstream river corridor. The three-dimensional voxel reconstruction, constrained by the mapped source boundary (Fig. 2) and three reference surfaces, defines the geometry and substantial volume of the released rock-ice body (Fig. 3B). This establishes the large mass involved in the initial failure.

The combination of substantial released mass, pronounced topographic relief and confined valley geometry indicates considerable gravitational energy available for rapid downslope transport. This energetic motion is captured by successive video frames showing the rapid advance of a dense, dust-bearing avalanche front within seconds (Fig. 3C1-C3). The extensive dust cloud reflects intense material disturbance during descent, while a subsequent frame records continued secondary rock-ice fall after the initial passage (Fig. 3C4). Together, the reconstructed terrain, source rock-ice body and direct video observations establish the conditions for highly mobile, energetic mass transport through the confined valley. As the moving debris entered the river corridor, its momentum and interaction with channel materials provided a physical pathway for the entrainment and downstream displacement of pre-existing river water. These observations therefore support the proposed transition from an initial rock-ice avalanche to a cascading debris-flow and flood process, providing the physical basis for the subsequent quantitative assessment of river-water mobilization and downstream flood volume.

Transformation into a debris-flow flood cascade

The reconstructed cascade reveals a progressive transformation of material composition and energy transfer from the initial rock-ice avalanche to the downstream flood (Fig. 4A). During rapid descent, the released rock-ice mass fragmented into large rock blocks and granular debris, which entrained loose sediments and channel deposits along the propagation corridor. The resulting dense debris flow remained dominated by solid materials, whose considerable momentum drove intense interactions with the underlying riverbed and pre-existing water. As illustrated in Fig. 4A1, the advancing debris mass scoured channel deposits, displaced river water and transferred momentum to the surrounding water, accelerating its downstream redistribution. As coarse materials progressively deposited, the moving mixture evolved into a hyperconcentrated flow and ultimately a water-dominated flood surge that continued beyond the principal debris-deposition zone. This sequence illustrates the transfer of gravitational energy through fragmentation, sediment entrainment and water mobilization,

157 transforming a localized slope failure into a far-reaching flood cascade. The underlying mechanisms
158 of granular motion, erosion and momentum transfer are consistent with previous experimental and field
159 investigations[36,37,38], as well as observations of rock-avalanche-generated sediment flows[39] and the
160 Chamoli disaster[4].
161 The spatial reconstruction further establishes the propagation pathway and the potential extent of
162 debris-driven water mobilization (Fig. 4B). KDFIM-derived mapping identifies the affected river
163 corridor and its flow-depth distribution[40,41], while DEM-based cumulative-energy analysis constrains
164 the downstream reachability of the moving material according to established routing and friction
165 principles[36,42,43,44,45]. The resulting critical-friction field delineates the energetically reachable corridor,
166 with finite values of $\mu_{crit} > 0.10$ defining the adopted spatial domain for solid-material influence under
167 the specified friction constraint[36,42,43,44,45]. This physically constrained domain identifies the river
168 reaches potentially exposed to direct debris interaction, providing the spatial basis for estimating the
169 pre-existing water available for mobilization. The recorded flood passage through the Bhote Koshi and
170 Trishuli valleys further establishes the temporal continuity of downstream propagation towards
171 Devghat[31,46].
172 Independent hydrological observations provide evidence for the above spatial reconstruction. Water
173 levels in the Kali Gandaki at Kota Gaon and Marsyangdi at Bimalnagar remained relatively stable
174 during the event, without a corresponding flood pulse (Fig. 4B)[46]. In contrast, Devghat recorded a
175 pronounced flood surge following the documented passage through the avalanche-affected Trishuli
176 corridor[31]. This spatial contrast, together with the observed propagation sequence, identifies the
177 upstream rock-ice avalanche cascade as the driver of the Devghat flood anomaly.
178 The reconstructed water inventory provides a quantitative test of the above mechanism. Hydraulic
179 information from the UT-1 Disaster Management Plan[47], combined with KDFIM-derived pre-event
180 water coverage, constrains the volume of river water within the debris-reachable corridor.

Independently, the reconstructed source composition defines the maximum potential meltwater supply[34]. Even under complete melting, source ice accounts for only approximately 53% of the observed excess floodwater, demonstrating that ice melting alone is insufficient to explain the downstream response. Combining the source-ice meltwater limit with the estimated corridor-water inventory yields an available water volume of $(14.42 \pm 0.80) \times 10^6$ m³, closely matching the independently derived Devghat excess[31] of 13.57×10^6 m³. The small difference between these estimates supports the volumetric feasibility of debris-driven river-water mobilization under the adopted melting and water-delivery assumptions.

Together, the reconstructed material transformations, spatially constrained debris reachability, tributary observations and downstream water-volume agreement provide converging evidence for the proposed flood-amplification mechanism. The initial rock-ice collapse supplied the mass and gravitational energy for rapid debris transport, while interactions with the river corridor enabled the mobilization and downstream redistribution of pre-existing water. This coupling between solid-material transport and river-water mobilization provides a physical explanation for how a localized high-mountain slope failure generated a destructive flood extending far beyond the initial collapse area.

Discussion

The observational comparisons provide quantitative evidence on the reconstructed Langtang Lirung rock-ice avalanche and its downstream flood response. By using a single source-volume and composition parameterization, the reconstructed mass and potential water inventory can be evaluated against independently acquired seismic and hydrological observations. The composition sensitivity analysis (Fig. 5) shows that the UAV-derived rock-to-ice ratio of 9:1 produces the smallest absolute discrepancies in both predicted seismic magnitude and available floodwater volume among the nine tested scenarios. Increasing the ice fraction progressively reduces the predicted magnitude while

substantially increasing the potential meltwater supply. Even when the rock-to-ice ratio shifts to 8:2, the predicted seismic magnitude changes only slightly, whereas the estimated available water volume exceeds the observed excess floodwater volume by more than 50%. This contrasting sensitivity demonstrates that the hydrological comparison provides particularly strong evidence on the assumed ice fraction, whereas the seismic comparison primarily evaluates the plausibility of the reconstructed moving mass. The agreement of both comparisons under the same source configuration strengthens the consistency of the reconstruction.

More importantly, the reconstructed cascade reveals how the initial gravitational energy and substantial rock-ice mass can drive downstream flood amplification through interactions with materials and water along the river corridor. During rapid descent, fragmentation and sediment entrainment transformed the initial avalanche into a dense debris flow capable of scouring channel deposits and transferring momentum to pre-existing river water. The resulting displacement and acceleration of river water concentrated part of the available water into a downstream-propagating surge, allowing the flood to extend beyond the principal deposition zone of coarse debris. This mechanism explains why the downstream flood response cannot be attributed to source-ice melting alone. The reconstructed corridor-water inventory, when combined with the maximum source-ice meltwater supply, closely approaches the independently estimated Devghat excess, with a central difference of only 6.30%. This quantitative correspondence supports the feasibility of debris-driven river-water mobilization as a major component of the cascading flood mechanism.

Comparisons with other Himalayan disasters place this mechanism within a broader context of cascading hazard amplification. During the 2021 Chamoli disaster, approximately 20% of the released material consisted of ice, and melting contributed to the transformation of the initial rock-ice avalanche into a highly mobile sediment-laden flow[4]. In the 2023 Sikkim disaster, the release of approximately 50×10^6 m³ of lake water was accompanied by extensive downstream erosion involving approximately

270×10^6 m^3 of sediment[48]. Although these events involved different initial water sources and flow-transformation pathways, they demonstrate how interactions with stored water and erodible valley materials can substantially extend the consequences of an initial disturbance. The Langtang Lirung cascade adds a distinct perspective by quantitatively examining the potential contribution of pre-existing river water, alongside source-ice melting. Its principal contribution lies in connecting this corridor-water inventory to both the reconstructed source mass and the downstream flood hydrograph through independent observational constraints.

The Langtang Lirung disaster demonstrates how a localized rock-ice avalanche can evolve into a far-reaching flood cascade through the coupled transport of solid debris and river water. By combining source reconstruction with independent seismic and hydrological observations, this study constrains both the initial release and the potential water available for downstream flood formation. The results show that source-ice melting alone is insufficient to account for the observed floodwater excess, while mobilization of pre-existing river water provides a quantitatively plausible explanation for the additional volume. This source-to-flood framework advances the understanding of high-mountain disaster amplification and highlights the need to incorporate river-water storage, sediment availability and downstream exposure into assessments of cascading hazards. Under global warming, the retreat of snow and glacier ice progressively reduces slope support and weakens ice-bonded rock masses. Extreme rainfall and major earthquakes can disturb these increasingly unstable slopes, increasing the risk of large cascading disasters across the Himalaya-Hindu Kush region. Connected river corridors transmit these hazards across national borders, making joint source-and-corridor hazard surveys, shared satellite, seismic and hydrological observations, and coordinated regional preparedness essential.

Methods

We reconstructed the source mass and available floodwater from imagery, terrain and external hydraulic information, then compared these outputs with separately acquired USGS seismic and Devghat discharge records (Fig. 1). The calculations and observational benchmarks are described below.

Three-stream design and separation of evidence

Stream A calculates source mass, long-period magnitude and available water using a single, well-defined set of source-volume and rock-to-ice ratio parameters. Stream B provides the USGS catalogue magnitude; Stream C calculates excess volume solely from the Devghat hydrograph. These observational benchmarks (B and C) do not enter the forward inventory equations.

Data sources and spatiotemporal characteristics

(1) Satellite imagery. Copernicus/ESA Sentinel-2 MultiSpectral Instrument (MSI) imagery acquired on 12 and 24 August 2026 provides the regional basemap and pre-failure source observations, respectively. Landsat-9 Operational Land Imager-2 (OLI-2) imagery acquired on 26 August 2026 records the post-collapse scar. Historical imagery accessed through Google Earth and dated 10 October 2017 provides the earlier structural view. Sentinel-2 and Landsat product specifications and access are provided by the Copernicus Data Space Ecosystem (https://dataspace.copernicus.eu/) and USGS EarthExplorer (https://earthexplorer.usgs.gov/), respectively. Post-event SAR imagery provided by the Changsha Tianyi Research Institute and Gaofen (GF) satellite imagery obtained from the Land Satellite Remote Sensing Application Center, Ministry of Natural Resources, were additionally used with KDFIM to reconstruct the flood-affected extent and inundation depth.

(2) Elevation data and derived products. Elevation data were obtained from the Copernicus Digital Elevation Model (COP-DEM GLO-30), which provides global elevation information (https://doi.org/10.5270/ESA-c5d3d65). The elevation data were resampled to a 10m analysis grid.

KDFIM was implemented on this common 10m grid to integrate the multi-source observations and derive flood extent and depth. All derived raster products in this study, including the source-reconstruction, reachability, water-mask, flood-extent and depth layers, were output at 10m grid spacing. This harmonized output spacing supports cell-wise integration and water-volume accounting. **(3) Seismic and hydrological observations.** The USGS earthquake catalogue provides the 26 August 2026 landslide event us7000tbwb, including its location, origin time and reported magnitude. Devghat discharge observations for 26 August 2026 were transcribed from the flood technical report issued by the Flood Forecasting Division, Hydrology and Water Resources Research Center, Water and Energy Commission Secretariat, Government of Nepal. The Centre of Hydrology and Water Resources Research Assessment Report II supplies the same-day water-level records for Kali Gandaki at Kota Gaon and Marsyangdi at Bimalnagar.

Stream A: forward source-to-river reconstruction

Source volume and mass

The three-dimensional source geometry was reconstructed from the DEM, the imagery-derived failure footprint (Fig. 2B-E) and the three reference surfaces a, b and c in Fig. 3B. The mapped footprint constrains the lateral extent of the failed body, while the spatial relationship between the DEM and the reference surfaces constrains its reconstructed vertical extent. We discretized this geometry into vertical voxel columns[49] and integrated their positive thicknesses over valid cells within the source footprint:

$$V_s = \sum_j I_j h_j A_j \quad (1)$$

where V_s is source volume; h_j and A_j are the reconstructed vertical thickness and ground area of voxel j, respectively; I_j equals 1 for valid positive-thickness cells within the source footprint and 0 otherwise.

The positive voxels yield $V_s = 78.37 \times 10^6 \mathrm{m}^3$. UAV interpretation gives a rock:ice volume ratio of 9:1. Mixture mass and density are:

$$m = \rho_{\mathrm{mix}} V_{\mathrm{s}}, \rho_{\mathrm{mix}} = f_i \rho_i + (1 - f_i)\rho_r \quad (2)$$

where $f_{\mathrm{i}} = 0.10$ is the source ice volume fraction, and $\rho_{\mathrm{i}} = 917$ kg m^{-3} and $\rho_r = 2700$ kg m^{-3} are ice and rock densities, respectively[34]. The resulting mixture density is 2.52×10^3kg m^{-3} and source mass m is 1.98×10^{11}kg.

Forward seismic scaling

The empirical landslide relations of Ekström and Stark[35] convert moving mass to maximum force and long-period magnitude:

$$\frac{m}{10^{12}\mathrm{kg}} \approx 0.54\hat{F}, \hat{F} = \frac{F_{\max}}{10^{12}\mathrm{N}} \quad (3)$$

$$M_{\mathrm{SW}} = 5.40 + 0.45\log_{10}\hat{F} \quad (4)$$

where $\hat{F}$ is maximum force normalized by 10^{12}N and M_{SW} is the predicted long-period magnitude. The adopted mass gives $\hat{F} = 0.37$, $F_{max} = 3.66 \times 10^{11}$N and $M_{SW} = 5.20$. A factor-of-two mass perturbation gives a magnitude range of 5.07-5.34.

DEM-constrained reachability

We applied KDFIM to pre- and post-event satellite imagery to delineate the horizontal extent of the affected river corridor and reconstruct its inundation-depth distribution[40,41]. These products define the spatial domain and characterize the vertical extent of the disaster impacts. We aligned the mapped corridor with the DEM and restricted the reachability calculation to this domain. Eight-neighbour cell connections define the routing network, and Dijkstra's algorithm identifies the shortest horizontal predecessor paths[42]. Elevations sampled from the DEM along these paths provide the elevation drop

and cumulative horizontal distance used to calculate the critical effective friction coefficient. The source reference elevation is volume-weighted:

$$z_0 = \frac{\sum_i z_i h_i A_i}{\sum_i h_i A_i} \quad (5)$$

where z_i, h_i and A_i denote source-cell elevation, reconstructed vertical thickness and ground area, respectively. Along each path, the cumulative-energy threshold is:

$$\mu_{\text{crit}}(s) = \min_{0<\ell\le s}\{\frac{z_0 - z(\ell)}{L_h(\ell)}\} \quad (6)$$

where $z(\ell)$ is path elevation and $L_h(\ell)$ is cumulative horizontal distance, including the source-centroid-to-corridor entry distance. The running minimum over all upstream path positions gives the greatest constant effective Coulomb friction coefficient allowing continuous reachability from rest[36,43,44]. This threshold screens energetic reachability within the prescribed corridor; finite, non-zero cells with μ_{crit} > 0.10 define the water-inventory domain. The effective-friction coefficient of 0.10 was adopted to delineate the maximum transport extent of debris flow and sediment along the mapped corridor. Cells satisfying the reachability criterion under Equation 6 were retained as the potential maximum runout domain. Such a low effective resistance is physically plausible for highly mobile rock-ice avalanches and debris flows, particularly where water availability, icy substrates and confined flow paths enhance mobility[14,50].

Pre-event corridor-water inventory

The pre-event optical water index follows the Spectral Knowledge-Driven Water Index (SKDWI) formulation in KDFIM[41]:

$$SKDWI = \frac{Green - NIR - SWIR2}{Green + NIR}. \quad (7)$$

where Green, NIR and SWIR2 denote surface reflectance in the green, near-infrared and second shortwave-infrared bands, respectively.

KDFIM corridor and water products[40], incorporating optical-SAR fusion and physics-constrained gap filling[41], were aligned on a common raster grid. Within the reachability domain, finite SKDWI values identify pre-event water[41]. Water area and storage are:

$$V_{\text{corridor}} = A_w d, A_w = 100 \sum_i W_i \quad (8)$$

where W_i is the binary water mask, each cell represents 100m^2, A_w is mapped water area and d is assigned mean depth. A_w = 1.61 × 10^{6}m^2. Depths of 4.00, 4.50 and 5.00m, informed by hydraulic information in the Disaster Management Plan for the Upper Trishuli-1 Hydropower Project (UT-1)[47], give inventories of 6.43, 7.24 and 8.04 × 10^{6}m^3. The central value (7.24 ± 0.80) × 10^{6}m^3 represents depth-scenario uncertainty.

Source-ice meltwater and available water

Mass conservation converts source ice to its liquid-water equivalent:

$$V_{\text{melt}} = \frac{\chi \rho_i f_i V_{\text{s}}}{\rho_w}, V_{\text{ice}} = f_i V_{\text{s}}, M_i = \rho_i f_i V_{\text{s}} \quad (9)$$

where V_{ice} and M_i are source-ice volume and mass, χ is melt fraction and ρ_w = 1000kg m^{-3}. Post-event field observations revealed no obvious residual ice in the affected area, providing observational support for considering complete source-ice melting. Accordingly, we adopted complete melting (χ = 1) as an upper-bound scenario, with V_{ice} = 7.84 × 10^{6}m^3 and V_{melt} = 7.19 × 10^{6}m^3, the latter representing the upper limit of the source-ice contribution to downstream flooding. Adding central corridor-water storage gives $V_{available} = V_{melt} + V_{corridor}$ = (14.42 ± 0.80) × 10^{6}m^3.

Stream B: USGS seismic benchmark

The USGS landslide event us7000tbwb reports a magnitude of 5.20 with catalogue type ms_vx[29]. This independently acquired value is compared with the forward long-period estimate.

360 **Stream C: Devghat excess volume**

361 Devghat discharge was transcribed from the 26 August 2026 technical report[31]. We used the first
362 observation, $Q_0 = 3.09 \times 10^3 m^3 s^{-1}$ at 14:10, as the operational baseline. Impulsive water disturbances
363 can generate wave crests and subsequent negative-phase fluctuations, and negative surges can lower
364 the local water surface[51,52]. Flood-wave propagation also produces peak attenuation and hydrograph
365 deformation[53]. A post-wave minimum can therefore reflect a transient hydraulic response and is not
366 used as the undisturbed reference. We adopt the station discharge observed before the recorded rise as
367 the reference for evaluating the positive discharge anomaly. Linear interpolation between 17:20 (3.22
368 $\times 10^3 m^3 s^{-1}$) and 17:30 ($3.00 \times 10^3 m^3 s^{-1}$) gives the return time t_e = 17:25:49. The excess volume, defined
369 here as the cumulative volume of discharge above the baseline over the event duration, is:

370 $$\Delta V_{\mathrm{D}} = \int_{t_0}^{t_e} (Q(t) - Q_0)\, dt \tag{10}$$

371 $$\Delta V_{\mathrm{D}} \approx \sum_j \frac{e_j + e_{j+1}}{2} \delta \mathrm{t}_j \tag{11}$$

372 where $Q(t)$ is discharge, $e_j = Q_j - Q_0$, and δt_j is the interval between observations. Trapezoidal
373 integration over 1.18×10^4s gives $\Delta V_D = 13.57 \times 10^6 m^3$; both $5.85 \times 10^3 m^3 s^{-1}$ observations at 16:00
374 and 16:10 are retained. Times follow the report's local-time convention.

375 **Paired validation**

376 We evaluated the source reconstruction using the difference between the forward-predicted magnitude
377 and the USGS value. We assessed the water budget using the signed difference between the calculated
378 available water and the Devghat excess, expressed as a percentage of the observed excess. The
379 maximum source-ice contribution was calculated by dividing complete-melt water yield by the
380 observed excess. Water-volume amplification was calculated by normalizing the predicted and
381 observed water volumes by that meltwater yield.

Data availability

The data supporting the findings of this study are publicly available at https://gip.csu.edu.cn/info/1484/7794.htm.

Code availability

The source code supporting the findings of this study is publicly available at https://gip.csu.edu.cn/info/1484/7794.htm.

Acknowledgements

This study was supported by the National Key Research and Development Program of China under Grant 2023YFE0208000. We thank Heimu for kindly providing the UAV footage used in this study, originally shared via Douyin (the Chinese counterpart of TikTok).

Author contributions

Zhijun Jiao: manuscript writing, methodology design, visualization and analysis. Suraj Gautam and Raju Thapa: hydrological data validation, provision of local information and manuscript review. Zhimei Zhang: assistance with manuscript writing and data curation. Pengtianhao Wu: hydrological analysis and manuscript revision. Zichen Yue and Qiqi Zhang: assistance with analysis. Wenfei Mao: discussion of the mechanism. Bishal Nath Upreti and Meen B. Poudyal Chhetri: hydrological data validation, provision of local information and manuscript review. Lixin Wu: conceptualization, supervision, funding acquisition, comprehensive analysis, data curation, manuscript review and language editing.

Competing interests

The authors declare no competing interests.

References

1. Fischer, L., Purves, R. S., Huggel, C., et al. On the influence of topographic, geological and cryospheric factors on rock avalanches and rockfalls in high-mountain areas. *Nat Hazards Earth Syst Sci* **12**, 241-254 (2012). https://doi.org/10.5194/nhess-12-241-2012

2. Gruber, S., et al. Review article: Inferring permafrost and permafrost thaw in the mountains of the Hindu Kush Himalaya region. *Cryosphere* **11**, 81-99 (2017). https://doi.org/10.5194/tc-11-81-2017

3. Kirschbaum, D., et al. The state of remote sensing capabilities of cascading hazards over High Mountain Asia. *Front Earth Sci* **7**, 197 (2019). https://doi.org/10.3389/feart.2019.00197

4. Shugar, D. H., et al. A massive rock and ice avalanche caused the 2021 disaster at Chamoli, Indian Himalaya. *Science* **373**, 300-306 (2021). https://doi.org/10.1126/science.abh4455

5. Hugonnet, R., McNabb, R., Berthier, E., et al. Accelerated global glacier mass loss in the early twenty-first century. *Nature* **592**, 726-731 (2021). https://doi.org/10.1038/s41586-021-03436-z

6. Bhattacharya, A., Bolch, T., Mukherjee, K., et al. High Mountain Asian glacier response to climate revealed by multi-temporal satellite observations since the 1960s. *Nat Commun* **12**, 4133 (2021). https://doi.org/10.1038/s41467-021-24180-y

7. Miles, E. S., McCarthy, M., Dehecq, A., et al. Health and sustainability of glaciers in High Mountain Asia. *Nat Commun* **12**, 2868 (2021). https://doi.org/10.1038/s41467-021-23073-4

8. Nie, Y., Pritchard, H. D., Liu, Q., et al. Glacial change and hydrological implications in the Himalaya and Karakoram. *Nat Rev Earth Environ* **2**, 91-106 (2021). https://doi.org/10.1038/s43017-020-00124-w

9. Zhang, T., Wang, W., Shen, Z., et al. Increasing frequency and destructiveness of glacier-related slope failures under global warming. *Sci Bull* **69**, 30-33 (2024). https://doi.org/10.1016/j.scib.2023.09.042

10. Clarke B, Zachariah M, Davies B, et al. Rapid warming in the Himalaya exacerbates geohazard cascades beyond adaptation limits. World Weather Attribution Scientific Report No. 92; 2026. https://doi.org/10.25560/136420

11. Zhuang, Y., Dawadi, B., Steiner, J., et al. An earthquake-triggered avalanche in Nepal in 2015 was exacerbated by climate variability and snowfall anomalies. *Commun Earth Environ* **5**, 465 (2024). https://doi.org/10.1038/s43247-024-01624-z

12. Kääb, A., Aga, J., Treichler, D., et al. Recent giant detachment of a glacier on the Tibetan plateau provoked by its frozen tongue. *Commun Earth Environ* **7**, 74 (2026). https://doi.org/10.1038/s43247-025-03125-z

13. Kang, J., Lucas, A., Mangeney, A., et al. Frictional weakening in the highly mobile 2025 Blatten rock and ice avalanche in Switzerland. *Commun Earth Environ* **7**, 722 (2026). https://doi.org/10.1038/s43247-026-03983-1

14. Schneider, D., Huggel, C., Haeberli, W., et al. Unraveling driving factors for large rock-ice avalanche mobility. *Earth Surf Process Landf* **36**, 1948-1966 (2011). https://doi.org/10.1002/esp.2218

15. Vaidya, R. A., Molden, D. J., Shrestha, A. B., et al. The role of hydropower in South Asia's energy future. *Int J Water Resour Dev* **37**, 367-391 (2021). https://doi.org/10.1080/07900627.2021.1875809

16. Taylor, C., Robinson, T. R., Dunning, S., et al. Glacial lake outburst floods threaten millions globally. *Nat Commun* **14**, 487 (2023). https://doi.org/10.1038/s41467-023-36033-x

17. Zhang, T., Wang, W., An, B., et al. Enhanced glacial lake activity threatens numerous communities and infrastructure in the Third Pole. *Nat Commun* **14**, 8250 (2023). https://doi.org/10.1038/s41467-023-44123-z

18. Zhang, T., Wang, W., Kougkoulos, I., et al. High frequency of moraine-dammed lake outburst floods driven by global warming. *Nat Commun* **16**, 11173 (2025). https://doi.org/10.1038/s41467-025-67650-3

19. Poudyal Chhetri, M. B. Downstream impact of melting glaciers: climate change in Nepal and beyond. In: Singh A, Fernando RLS, Haran NP, editors. Development in coastal zones and disaster management. Singapore: Palgrave Macmillan; 2020. p. 293-301. https://doi.org/10.1007/978-981-15-4294-7_20

20. Rick, B., McGrath, D., McCoy, S. W., et al. Unchanged frequency and decreasing magnitude of outbursts from ice-dammed lakes in Alaska. *Nat Commun* **14**, 6138 (2023). https://doi.org/10.1038/s41467-023-41794-6

21. Hata, S., Sugiyama, S. & Heki, K. Abrupt drainage of Lago Greve, a large proglacial lake in Chilean Patagonia, observed by satellite in 2020. Commun Earth Environ 3, 190 (2022). https://doi.org/10.1038/s43247-022-00531-5

22. Emmer, A. Understanding the risk of glacial lake outburst floods in the twenty-first century. Nat Water 2, 608-610 (2024). https://doi.org/10.1038/s44221-024-00254-1

23. Veh, G. et al. Progressively smaller glacier lake outburst floods despite worldwide growth in lake area. Nat Water 3, 271-283 (2025). https://doi.org/10.1038/s44221-025-00388-w

24. Allen, S. K., Zhang, G., Wang, W., et al. Potentially dangerous glacial lakes across the Tibetan Plateau revealed using a large-scale automated assessment approach. Sci Bull 64, 435-445 (2019). https://doi.org/10.1016/j.scib.2019.03.011

25. Sattar, A., Allen, S., Mergili, M., et al. Modeling potential glacial lake outburst flood process chains and effects from artificial lake-level lowering at Gepang Gath Lake, Indian Himalaya. *J Geophys Res Earth Surf* **128**, e2022JF006826 (2023). https://doi.org/10.1029/2022JF006826

26. Büntgen, U., Oppenheimer, C., Farinotti, D., et al. The 2025 Blatten disaster in the Swiss Alps followed exceptional warming and highlights the vulnerability of people and heritage in glaciated landscapes. *Commun Earth Environ* **6**, 994 (2025). https://doi.org/10.1038/s43247-025-02994-8

27. Dandabathula, G., Ghatage, O. S., Roy, S., et al. Ice-patch collapse and early-warning implications from a Himalayan flash flood: emerging cryo-hydrological hazards under deglaciation. *npj Nat Hazards* **3**, 24 (2026). https://doi.org/10.1038/s44304-026-00191-x

28. U.S. Geological Survey. 2026 Nepal debris avalanche and flash flood. Landslide Hazards Program (2026). https://www.usgs.gov/programs/landslide-hazards/science/2026-nepal-debris-avalanche-and-flash-flood

29. U.S. Geological Survey. M 5.2 Landslide, 55 km NW of Kodari, Nepal. Event us7000tbwb, 26 August 2026. https://earthquake.usgs.gov/earthquakes/eventpage/us7000tbwb/executive

30. National Disaster Risk Reduction and Management Authority. Rasuwa-Bhotekoshi flood: search, rescue and relief response. Situation Report No. 20, 21 September 2026, 19:00. Kathmandu: Government of Nepal; 2026.

31. Flood Forecasting Division, Hydrology and Water Resources Research Center, Water and Energy Commission Secretariat, Government of Nepal. Technical report on the '2083 Bhotekoshi-Trishuli-Narayani flood' (2026). English translation supplied with this study.

32. Mao, W., Wu, L., Singh, R. P., et al. Progressive destabilization and triggering mechanism analysis using multiple data for Chamoli rockslide of 7 February 2021. *Geomatics Nat Hazards Risk* **13**, 35-53 (2022). https://doi.org/10.1080/19475705.2021.2013960

33. Reddy, S. M., Searle, M. P. & Massey, J. A. Structural evolution of the High Himalayan Gneiss sequence, Langtang Valley, Nepal. *Geol Soc Lond Spec Publ* **74**, 375-389 (1993). https://doi.org/10.1144/GSL.SP.1993.074.01.25

34. Cuffey KM, Paterson, W. S. B. The physics of glaciers. 4th ed. Elsevier; 2010.

35. Ekström, G. & Stark, C. P. Simple scaling of catastrophic landslide dynamics. *Science* **339**, 1416-1419 (2013). https://doi.org/10.1126/science.1232887

496 36. Iverson, R. M. The physics of debris flows. *Rev Geophys* **35**, 245-296 (1997).
497 https://doi.org/10.1029/97RG00426
498 37. Gray, J. M. N. T., Tai, Y. C. & Noelle, S. Shock waves, dead zones and particle-free regions in
499 rapid granular free-surface flows. *J Fluid Mech* **491**, 161-181 (2003).
500 https://doi.org/10.1017/S0022112003005317
501 38. Pudasaini, S. P. & Krautblatter, M. The mechanics of landslide mobility with erosion. *Nat Commun*
502 **12**, 6793 (2021). https://doi.org/10.1038/s41467-021-26959-5
503 39. Mitchell, A., McDougall, S., Aaron, J., et al. Rock avalanche-generated sediment mass flows:
504 definitions and hazard. *Front Earth Sci* **8**, 543937 (2020). https://doi.org/10.3389/feart.2020.543937
505 40. Jiao, Z., Zhang, Z., Chen, B., et al. Knowledge-Driven Flood Intelligent Monitoring (KDFIM)
506 method: analyzing the Kakhovka Dam destruction incident. *IEEE J Sel Top Appl Earth Obs Remote*
507 *Sens* **18**, 19947-19960 (2025). https://doi.org/10.1109/JSTARS.2025.3594119
508 41. Jiao, Z., Wu, P., Chen, B., et al. Enabling seamless spatiotemporal flood monitoring via bridging
509 observational gaps with a case study on the 2024 Bangladesh flood. *Int J Appl Earth Obs Geoinf* **151**,
510 105412 (2026). https://doi.org/10.1016/j.jag.2026.105412
511 42. Dijkstra, E. W. A note on two problems in connexion with graphs. *Numer Math* **1**, 269-271 (1959).
512 https://doi.org/10.1007/BF01386390
513 43. Savage, S. B. & Hutter, K. The motion of a finite mass of granular material down a rough incline.
514 *J Fluid Mech* **199**, 177-215 (1989). https://doi.org/10.1017/S0022112089000340
515 44. Iverson, R. M. & Denlinger, R. P. Flow of variably fluidized granular masses across three-
516 dimensional terrain: 1. *Coulomb mixture theory. J Geophys Res Solid Earth* **106**, 537-552 (2001).
517 https://doi.org/10.1029/2000JB900329
518 45. Scheidegger, A. E. On the prediction of the reach and velocity of catastrophic landslides. *Rock*
519 *Mech* **5**, 231-236 (1973). https://doi.org/10.1007/BF01301796

520 46. Centre of Hydrology and Water Resources Research, Water and Energy Commission Secretariat,
521 Government of Nepal. Assessment Report II: Rasuwa-Bhote Koshi Flood Event, 2026 (2083). 13
522 September 2026. Section 5.3, Fig. 11; Section 5.5.
523 47. HECT Consultancy. Disaster Management Plan, Upper Trishuli-1 Hydropower Project, Rasuwa
524 District, Nepal (2017). IFC Project 35701. https://disclosures.ifc.org/project-
525 detail/ESRS/35701/upper-trishuli-1
526 48. Sattar, A., et al. The Sikkim flood of October 2023: Drivers, causes, and impacts of a multihazard
527 cascade. *Science* **387**, eads2659 (2025). https://doi.org/10.1126/science.ads2659
528 49. Liu, D., Peng, B., Wu, L., Wang, R., Yang, Y. & Xie, B. Flat voxel-based modelling, assessment
529 and visualization of urban underground space resource quality. *Int J Appl Earth Obs Geoinf* **113**,
530 102984 (2022). https://doi.org/10.1016/j.jag.2022.102984
531 50. Sosio, R., Crosta, G. B., Chen, J. H. & Hungr, O. Modelling rock avalanche propagation onto
532 glaciers. *Quat Sci Rev* **47**, 23-40 (2012). https://doi.org/10.1016/j.quascirev.2012.05.010
533 51. Reichstetter, M. & Chanson, H. Negative surges in open channels: physical and numerical
534 modeling. *J Hydraul Eng* **139**, 341-346 (2013). https://doi.org/10.1061/(ASCE)HY.1943-
535 7900.0000674
536 52. Mohammed, F. & Fritz, H. M. Physical modeling of tsunamis generated by three-dimensional
537 deformable granular landslides. *J Geophys Res Oceans* **117**, C11015 (2012).
538 https://doi.org/10.1029/2011JC007850
539 53. Paiva, R. C. D. & Lima, S. G. A simple model of flood peak attenuation. *Water Resour Res* **60**,
540 e2023WR034692 (2024). https://doi.org/10.1029/2023WR034692

Figures and figure legends

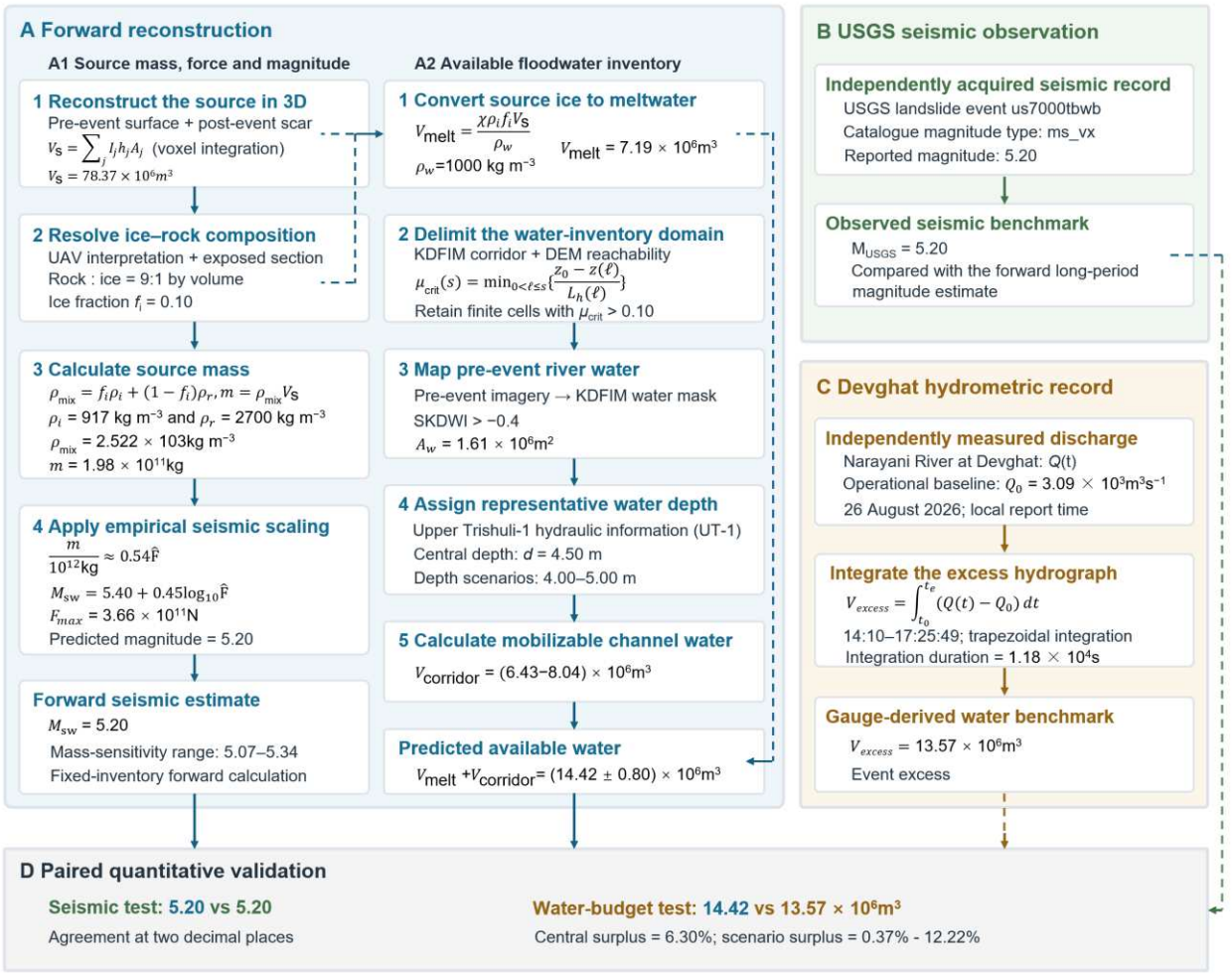


Fig.1 Three-stream workflow for source-to-river reconstruction and paired validation. (A1) Source geometry and UAV-derived rock:ice composition determine mass and the seismic estimate. (A2) Source-ice meltwater is added to corridor-water storage estimated from KDFIM water mapping, DEM-based reachability and 4.0-5.0m depth scenarios. (B) The USGS catalogue supplies the seismic benchmark. (C) Devghat discharge is integrated above an operational baseline to obtain excess flood volume. (D) The two comparisons test the reconstructed inventory against separate observations. Solid arrows show calculation sequences; dashed arrows indicate shared inputs or external comparisons.

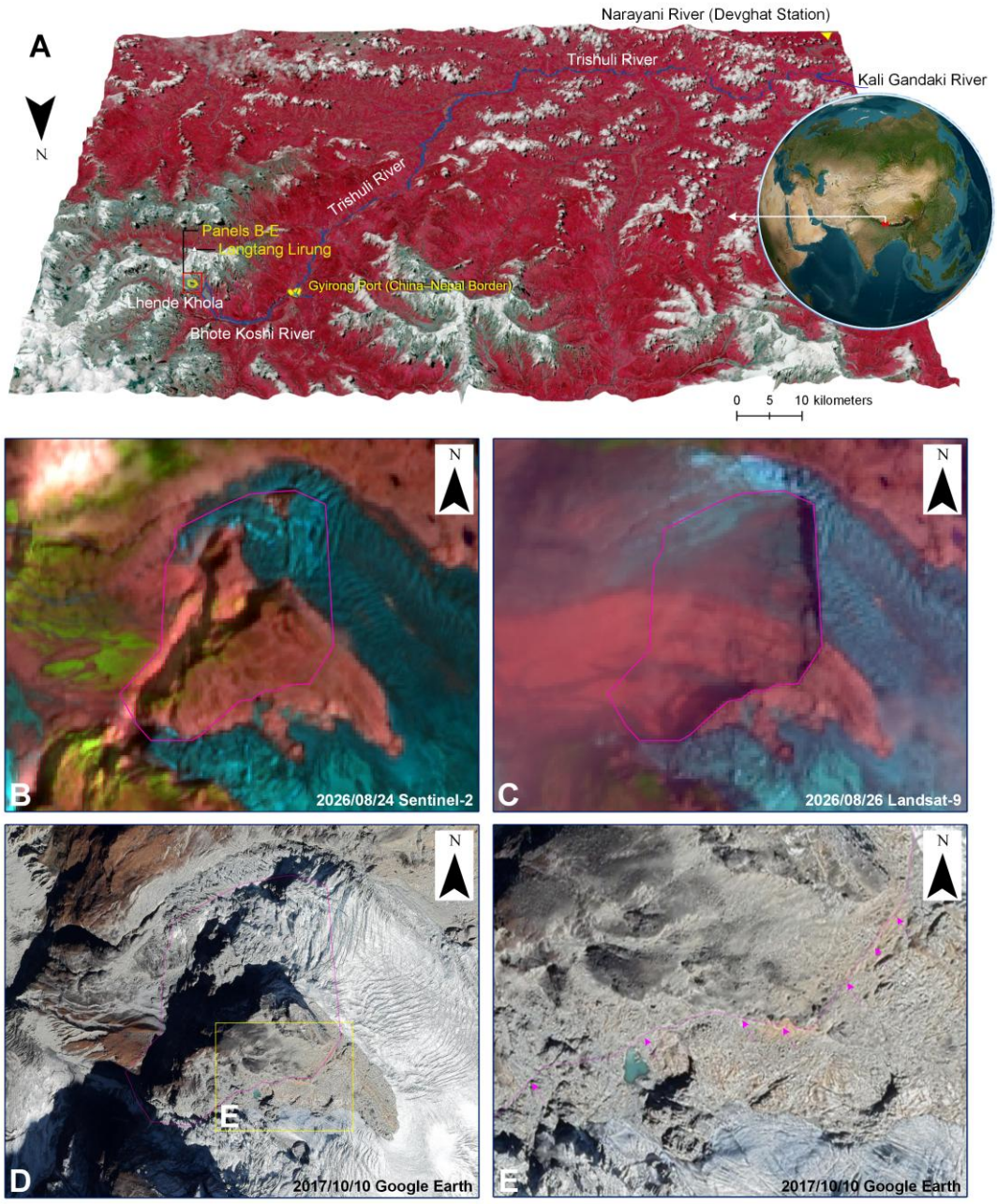
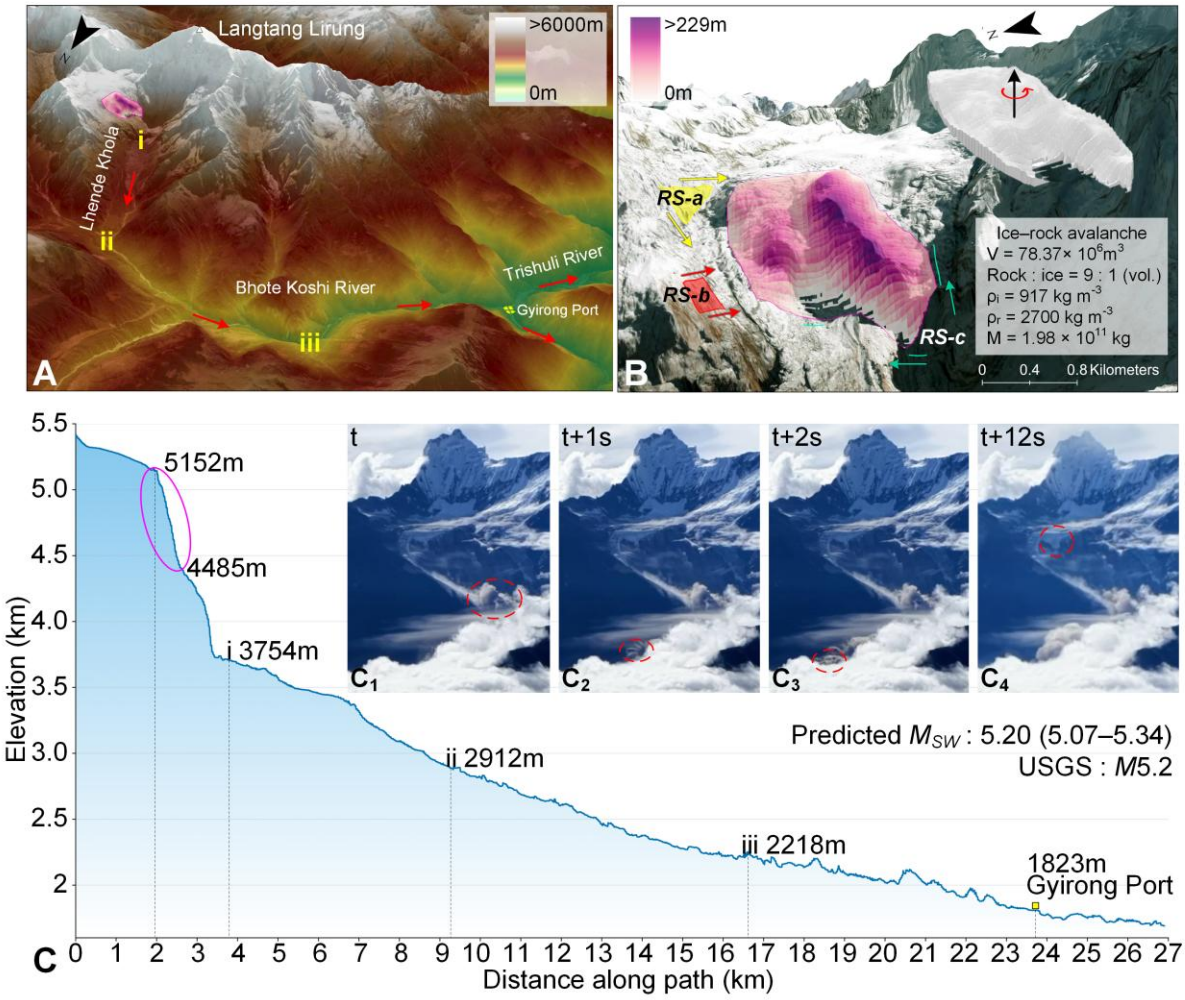


Fig.2 Regional setting, source-area changes and failure footprint of the 26 August 2026 Lirung rock-ice avalanche. (A) Sentinel-2 image acquired on 12 August 2026, showing the source area, mapped impact corridor, Gyirong Port at the China-Nepal border and the Devghat hydrometric station on the Narayani River. The inset shows the global location of the study area. (B) Pre-event Sentinel-2 image acquired on 24 August 2026, showing the intact source area. (C) Post-event Landsat-9 image acquired on 26 August 2026, revealing the newly exposed collapse scar used to delineate the source rock-ice body. (D) High-resolution Google Earth image acquired on 10 October 2017, showing the pre-existing fractured and weathered rock zone, with the reconstructed source boundary overlaid. (E) Enlarged view of the historical image, highlighting the close correspondence between the pre-existing fracture pattern and the reconstructed failure boundary.



560

561 **Fig.3 Source reconstruction and rapid downslope propagation of the Lirung rock-ice avalanche.** (A) Oblique
562 topographic view illustrating the propagation corridor from the source towards Gyirong Port, with locations i-iii
563 marking successive reaches along Lhende Khola and Bhote Koshi. (B) Three-dimensional reconstruction of the
564 released rock-ice body constrained by the mapped source footprint and three reference surfaces (RS-a, RS-b and RS-
565 c). (C) Longitudinal terrain profile showing the pronounced elevation drop from the source to the Gyirong Port
566 corridor. (C1-C3) Successive video frames capturing the rapid downslope movement of the dust-bearing avalanche
567 front within reach i-ii. (C4) A subsequent frame showing continued secondary rock-ice fall.

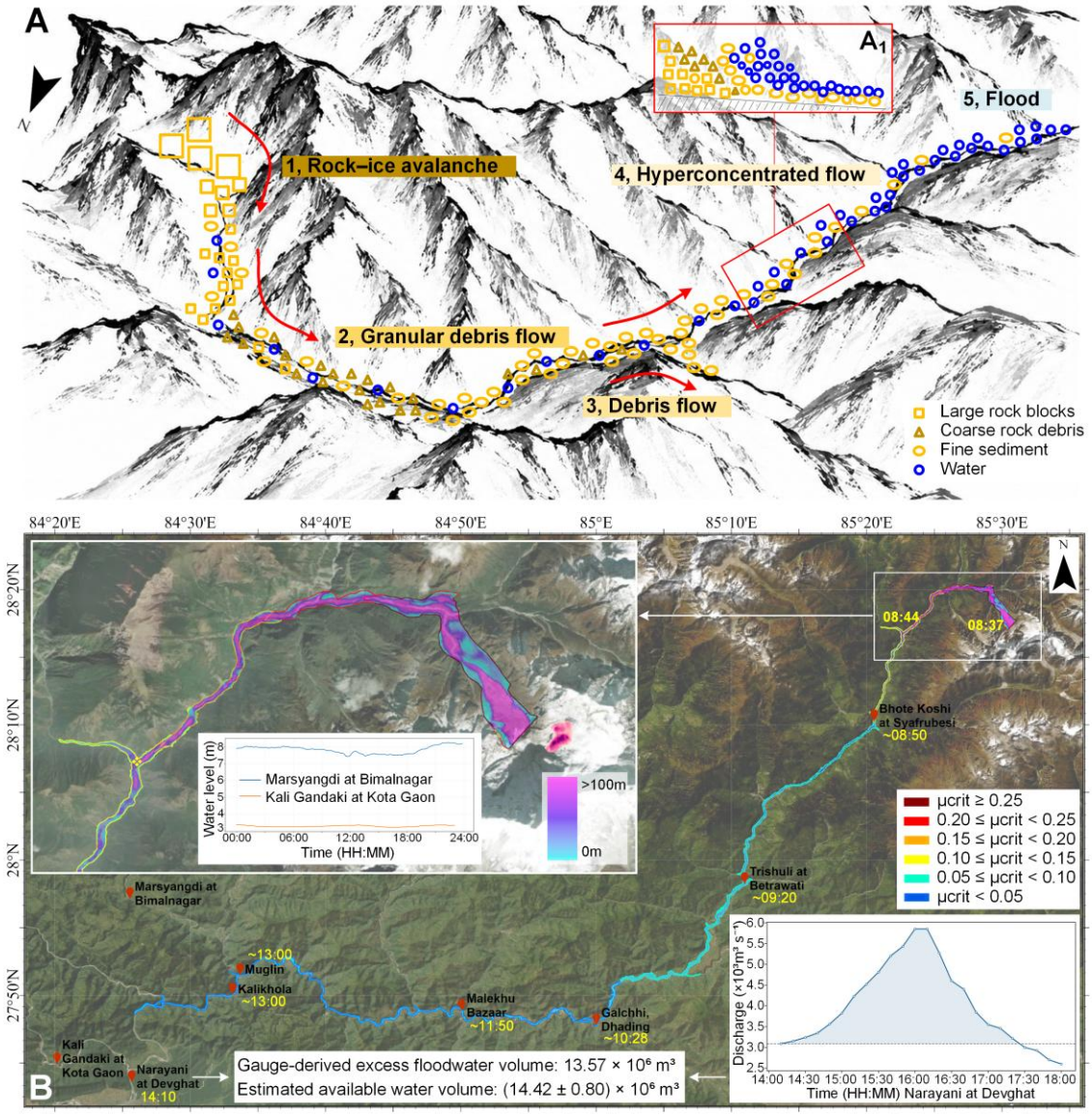
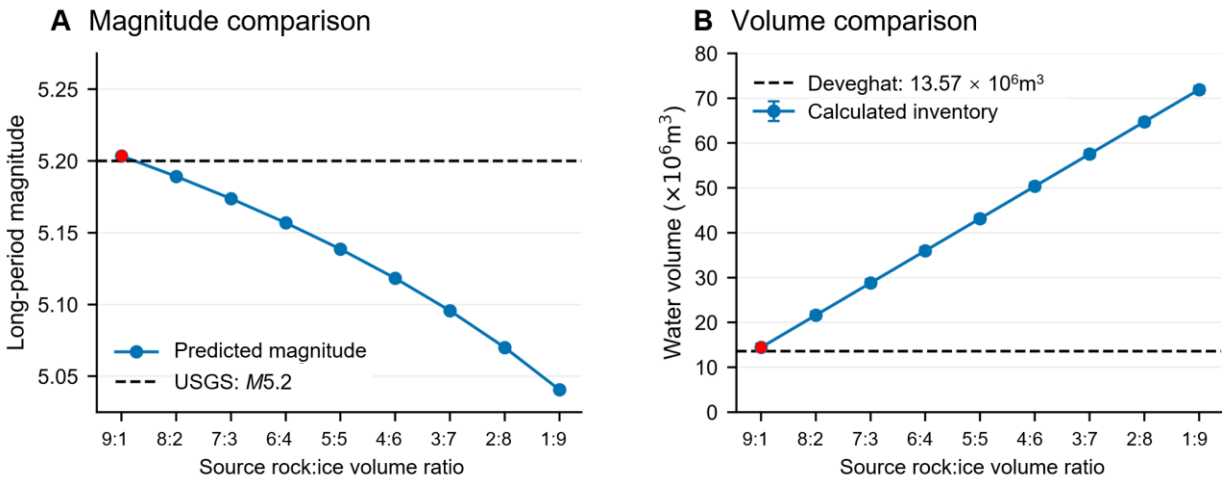


Fig.4 Cascade transformation, debris-driven river-water mobilization and downstream flood response. (A) Conceptual reconstruction of the progressive transformation from rock-ice avalanche (1) to granular debris flow (2), debris flow (3), hyperconcentrated flow (4) and flood (5). (A1) Schematic representation of the interaction between high-momentum debris and pre-existing river water, illustrating channel scouring, sediment entrainment and downstream water displacement. (B) Spatial and temporal reconstruction of the cascade, showing the propagation corridor, recorded flood passage times, flow-depth distribution and critical-friction field. Insets show the water-level records at Kali Gandaki and Marsyangdi and the Devghat discharge hydrograph. The reconstructed maximum available water volume is (14.42 ± 0.80) × 10^6 m^3, compared with an observed excess floodwater volume of 13.57 × 10^6 m^3.



578

579 **Fig.5 Sensitivity of predicted seismic magnitude and available floodwater volume to source rock–ice**
580 **composition.** Nine rock-to-ice volume ratios, ranging from 9:1 to 1:9, were evaluated using the same reconstructed
581 source volume and constituent densities under the complete-melting assumption. (A) Predicted long-period seismic
582 magnitude compared with the independently reported USGS magnitude (dashed line). (B) Estimated available water
583 volume, combining potential source-ice meltwater and pre-existing corridor-water storage, compared with the
584 Devghat excess floodwater volume (dashed line).